

Core–shell nanoscale precipitates in Al–0.06 at.% Sc microalloyed with Tb, Ho, Tm or Lu

Matthew E. Krug^a, Alexandra Werber^{a,b}, David C. Dunand^a, David N. Seidman^{a,c,*}

^a Northwestern University, Materials Science and Engineering, 2220 Campus Drive, Northwestern University, Evanston, IL 60208-3108, USA

^b Universität Karlsruhe, Kaiserstraße 12, 76131 Karlsruhe, Germany

^c Northwestern Center for Atom-Probe Tomography, 2220 Campus Drive, Evanston, IL 60208-3108, USA

Received 16 March 2009; received in revised form 27 August 2009; accepted 28 August 2009

Available online 1 October 2009

Abstract

The age-hardening response at 300 °C of Al–0.06Sc–0.02RE (at.%, with RE = Tb, Ho, Tm or Lu) is found to be similar to that of binary Al–0.08Sc (at.%), except that a shorter incubation period for hardening is observed, which is associated with nanoscale RE-rich Al₃(RE_{1–x}Sc_x) precipitates. In addition, Al–0.06Sc–0.02Tb (at.%) has a much lower peak microhardness than that of Al–0.08Sc (at.%) due to the small solubility of Tb in α -Al(Sc). Peak-age hardening occurs after 24 h, and is associated with a high number density of nanoscale Sc-rich Al₃(Sc_{1–x}RE_x) precipitates. Analysis by three-dimensional local-electrode atom-probe tomography shows that x increases with increasing atomic number, and that the REs partition to the core of the precipitates.

© 2009 Acta Materialia Inc. Published by Elsevier Ltd. All rights reserved.

Keywords: Rare earth; Precipitation; Microhardness; Atom-probe field-ion microscopy (AP-FIM); Aluminum alloys

1. Introduction

Small additions of Sc to Al result in the formation of a high number density (as high as 10^{22} m^{-3}) of elastically stiff Al₃Sc (L₁₂ structure) precipitates that are coherent with the α -Al matrix, which impart strength to the alloy [1–6]. On a per-atom basis, Sc has the greatest strengthening effect of any existing alloying addition to Al [7]. The Al₃Sc precipitates coarsen slowly up to ~ 300 °C, imparting good creep resistance in coarse-grained cast alloys [1–3,6,8–13].

Ternary additions to Al–Sc alloys improve mechanical properties by solid-solution strengthening as in the case of Mg [14–18], or by substituting for Sc in Al₃Sc precipitates as in the cases of Ti and Zr [19–22]. In addition to these transition metals, the late lanthanoids also exhibit substantial solubility (Gd–Ho) to complete solubility (Er–Lu) in Al₃Sc [23–25], as a result of possibly substituting

on the Sc sublattice in Al₃Sc [26]. An element that substitutes for Sc in Al₃Sc should have the following characteristics if it is to be effective for high-temperature applications: (i) to facilitate precipitation from a solid solution, it should have a solubility in α -Al on the order of hundreds of at. ppm at the alloy homogenization temperature, but low solubility at aging and service temperatures [27]; (ii) to limit the rate of precipitate coarsening, it should have a small diffusivity in α -Al; (iii) to increase creep resistance, it should increase the lattice parameter mismatch to maximize elastic interactions between precipitates and dislocations; and (iv) to decrease the price of the alloy, it should be less expensive than Sc. Many of these characteristics are exhibited by the late lanthanoids [24–26,28,29].

In a recent atom-probe tomography (APT) study of six ternary Al–0.06Sc–0.02RE alloys (RE = Y, Sm, Gd, Dy, Er or Yb; concentrations hereafter are in at.% unless otherwise noted), it was shown that REs substitute for Sc in the nanoscale L₁₂ trialuminide precipitates, resulting in an aging microhardness response at 300 °C generally similar to that of a binary Al–0.08Sc alloy with the same solute

* Corresponding author.

E-mail addresses: m-krug@northwestern.edu (M.E. Krug), d-seidman@northwestern.edu (D.N. Seidman).

concentration [30]. Several exceptions were noted. First, Al–Sc–Sm and Al–Sc–Gd alloys have lower peak strengths than Al–0.08Sc due to the lower solubility of these elements in Al₃Sc as compared to the other REs studied, and due to the precipitation of micron-scale Al–Sm precipitates at the grain boundaries in the Al–Sc–Sm alloy. Second, a very rapid initial increase in the microhardness of Al–Sc–Yb occurred, attributed to the experimentally observed clustering of Yb atoms at early aging times (including the as-quenched state). As compared to Sc, Yb has a diffusivity in Al at 300 °C that is three orders of magnitude greater [31], promoting rapid decomposition of the supersaturated solid-solution and growth of the precipitates.

In this study, we complete the above study by exploring the microhardness response and microstructural changes occurring during aging of ternary Al–0.06Sc–0.02RE alloys, where REs are the remaining four Al₃Sc-soluble late lanthanoids (Tb, Ho, Tm, Lu), which were not studied previously [30]. In this and the prior study, the small nominal RE concentration was chosen to increase the probability of achieving a single-phase α -Al state during homogenization, as the exact solubilities of these REs in Al are small but unknown. Tb and Ho are moderately expensive ($\sim 1/10$ the price of Sc) but only partly soluble in Al₃Sc, whereas Tm and Lu are more expensive ($\sim 1/3$ the price of Sc) but fully soluble in Al₃Sc [32]. The study of these unexplored ternary alloys is interesting both technologically, as substitution of Sc by RE reduces the cost of Al–Sc alloys, and scientifically, as it permits a more complete examination of trends among REs in dilute Al–Sc–RE alloys.

2. Materials and methods

Four Al–0.06Sc–0.02RE alloys (RE = Tb, Ho, Tm, Lu) were dilution-cast from 99.999% pure Al (Alcoa, Inc., Pittsburgh, PA), a 99.9% pure Al–1.3Sc master alloy (Ashurst Technology Ltd., Baltimore, MD, and KB Alloys, Inc., Reading, PA), and Al–1RE master alloys. The RE master alloys were produced by non-consumable electrode arc-melting from 99.999% pure Al and 99.9% pure RE metals (Stanford Materials, Aliso Viejo, CA). These were melted in a zirconia-coated alumina crucible in a resistively heated furnace at 750 °C. The thoroughly stirred melt was cast into a graphite mold preheated to 200 °C. The mold rested on a large ice-cooled copper-platen, and a propane flame heated the exposed cast metal at the top of the mold. These measures were employed to encourage directional solidification of the ingots, to promote a uniform composition near the mid-length of the cylindrical ingots, which have a diameter of approximately 1 cm and a length of approximately 10 cm, and to discourage the formation of shrinkage cavities. Chemical compositions of arc-melted master alloys and homogenized dilute alloys were measured by direct-current plasma mass-spectroscopy (DCPMS) by ATI Wah Chang (Albany, OR).

Specimens were removed from near the mid-length position of the cast ingots, where the composition was mea-

sured by DCPMS. The specimens were homogenized in air at 640 °C for 72 h and then water quenched to ambient temperature. Aging was performed at 300 °C for various times, and was terminated by a water quench to ambient temperature. Molten salt (NaNO₂–NaNO₃–KNO₃) baths were used for aging durations of 30 min or less to ensure rapid heat transfer, while longer aging experiments were performed in air. Vickers microhardness measurements were performed at ambient temperature using a 200 g load applied for 5 s on specimens ground to a 1 μ m surface finish. Twenty indentations per specimen were made including several grains.

Specimens for three-dimensional (3-D) local-electrode atom-probe (LEAP) tomography [33–35] were prepared by cutting blanks with a diamond saw to approximate dimensions of 400 μ m \times 400 μ m \times 1 cm. These were then electropolished to an atomically sharp point using a solution of 10% perchloric acid in acetic acid, followed by a second solution of 2% perchloric acid in butoxyethanol. The specimens were dissected on atom-by-atom and atomic-plane-by-plane bases employing a LEAP 3000X Si (Imago Scientific Instruments, Madison, WI) at 30 \pm 2 K using 1.5 nJ pulses of green laser light at a pulse repetition rate of 500 kHz (Appendix A), resulting in an effective pulse fraction of 15%. Three-dimensional tomographic reconstructions were created, and quantitative analyses of the data were performed using IVAS version 3.2.1 (Imago Scientific Instruments). The distance scale parallel to the long axis of a tip is calibrated using the low-index poles, where the atomic planes are resolvable. The reconstruction parameters were modified such that the measured interplanar spacing near the low-index poles matches to within 5% the correct value for Al. At least two of the following low-index poles were used for each dataset, depending on the orientation of the tip axis relative to the crystallographic orientation: $\langle 111 \rangle$, $\langle 002 \rangle$, $\langle 022 \rangle$, $\langle 113 \rangle$, $\langle 024 \rangle$ and $\langle 224 \rangle$. The distances in the orthogonal directions are verified by comparing the atomic density to the value for Al, employing a detection efficiency of 0.55. Evaporation-field values giving the correct reconstructed geometry varied between 11 and 16 V nm^{−1}. For electrical pulsing the value is 19 V nm^{−1} for Al at 78 K [36]. The smaller estimated values we obtain are probably due to tip heating [37], and also indicate that the degree of heating was variable due to differences in tip geometry, such as shank angle.

3. Results

3.1. Composition

The alloy compositions are displayed in Table 1. The bulk composition was measured by DCPMS for specimens in the as-homogenized condition, and corresponds to a volume of material ~ 0.3 cm³. Impurity concentrations for Fe and Si, which can alter the nucleation kinetics of the Sc- and RE-containing precipitates, were measured to be less than 50 at. ppm. The local composition measurements were

Table 1
Composition (at.%) of six Al–Sc–RE alloys, as determined by directly coupled plasma mass spectroscopy (DCPMS) and by LEAP tomographic spectroscopy.¹

Alloy	Bulk composition (DCPMS)			Local composition (LEAP)			
	Sc	RE	Sc + RE	Specimen aged 10 min		Specimen aged 24 h	
				Sc	RE	Sc	RE
Al–Sc ²	0.060(6)	–	0.060(6)	0.0571(8) ³	–	–	–
Al–Sc ²	0.082(6)	–	0.082(6)	0.086(1) ³	–	–	–
Al–Sc–Tb	0.054(2)	0.023(9)	0.076(9)	0.0564(6)	0.0032(2)	0.0529(6)	0.0024(2)
Al–Sc–Ho	0.054(4)	0.022(9)	0.076(9)	0.0608(6)	0.0065(2)	0.0624(6)	0.0083(2)
Al–Sc–Tm	0.055(2)	0.0170(2)	0.072(2)	0.0678(7)	0.0141(3)	0.0787(7)	0.0124(3)
Al–Sc–Lu	0.0532(6)	0.0172(2)	0.0704(6)	0.0660(6)	0.0217(3)	0.0734(7)	0.0156(3)

¹ Uncertainty corresponds to 2 standard deviations (SD), and is given in parenthesis after the least significant digits to which it applies.

² Data from Ref. [30].

³ LEAP spectroscopy (local composition) was performed on a specimen in the as-homogenized condition.

obtained by 3-D LEAP tomographic spectroscopy on specimens for two aging conditions, and correspond to a volume of approximately 10^6 nm^3 . The compositions of the datasets measured by 3-D LEAP tomography are calculated by dividing the number of atoms of each species by the total number of atoms in the dataset, making a correction for background subtraction in the mass-to-charge state (m/n) ratio spectra. The statistical uncertainty in concentration is reported as $2\sigma_c$, where σ_c is calculated as $\sqrt{C_i(1 - C_i)/N_{total}}$ [38]. Here, C_i is the atomic fraction of element i and N_{total} is the total number of atoms detected. As a baseline comparison, data from prior work [30], including binary Al–0.06Sc and Al–0.08Sc alloys, are also included in Table 1. For these binary alloys, the composition measurements by 3-D LEAP spectroscopy were conducted on specimens in the as-homogenized condition using electrical pulsing.

The RE concentrations for the Al–Sc–Tb and Al–Sc–Ho alloys are smaller when 3-D LEAP spectroscopy is used compared to DCPMS (Table 1). Despite the small concentrations of RE in these alloys (nominally 0.02), observation by scanning electron microscopy (SEM)/energy dispersive X-ray spectroscopy (EDX) in the as-homogenized condition revealed the presence of Sc- and RE-rich primary precipitates several micrometers in diameter, indicating that for Al–0.06Sc–0.02Tb and Al–0.06Sc–0.02Ho, the solute concentrations exceed the solubility limits of Sc + RE in α -Al at 640 °C. For comparison, the maximum solubilities of Sc, Yb and Er in binary Al–X alloys are 0.23 [39], 0.0248 [31] and 0.0461 [40], respectively. The two composition measurements of Al–Sc–RE alloys by 3-D LEAP spectroscopy were performed on specimens aged for 10 min and 24 h, which were separated by a distance of several centimeters in the casting of their origin, and illustrate the degree of variability in the casting composition, which is typically several tens of at. ppm (Table 1).

3.2. Microhardness evolution

Vickers microhardness is plotted as a function of aging time at 300 °C in Fig. 1. Data for the binary Al–Sc alloys

are from prior work. All of the alloys display the basic characteristics of precipitation-hardening behavior: (a) an incubation period; (b) an increase in microhardness during which second-phase precipitates nucleate from a supersaturated solid-solution and grow; (c) a period of maximum hardness; and (d) over-aging, characterized by a slow decrease in microhardness as the precipitates grow and coarsen. For all alloys, the addition of 0.02Sc or 0.02RE to an Al–0.06Sc alloy increases the maximum microhardness of the aged alloys, from ~ 350 HV to between 490 HV for Tb and 590 HV for Tm, and up to 630 HV for Sc. The maximum microhardness values of Al–Sc–Tm and Al–Sc–Lu are slightly less than that of Al–0.08Sc, in accordance with their total solute concentration, which is ~ 100 at. ppm. lower (Table 1). The peak microhardness values of the Al–Sc–Ho and especially the Al–Sc–Tb alloys are smaller than for the binary Al–0.08Sc alloy due to the small solubilities of these REs in α -Al, Table 1, which depletes the solid-solution and hence the precipitating phase of a significant fraction of the strengthening solute.

The substitution of 0.02Sc with a RE in Al–0.08Sc causes a decrease in the incubation time: Al–Sc–Tm begins age hardening after less than 30 s, and the other ternary alloys all exhibit unambiguous increases in hardness by 5 min. By comparison, Al–0.08Sc begins to age harden between 15 and 60 min. Furthermore, the ternary alloys display, to varying degrees, evidence of two distinct microhardness increase steps, with a first microhardness plateau between ~ 5 and 60 min, and a second plateau in microhardness occurring between ~ 2 and 24 h. The Al–Sc–Tm alloy is the only one whose age-hardening curve is sufficiently free of scatter to observe clearly a first distinct microhardness plateau between 5 and 15 min, and it also reaches a maximum microhardness most rapidly, after ~ 2 h. The binary Al–0.08Sc alloy reaches its microhardness maximum after ~ 6 h, as compared to ~ 4 h for Al–Sc–Lu, Al–Sc–Tb and Al–Sc–Ho. The sampling resolution in aging time is not sufficient to claim unambiguously a difference in the aging time to peak microhardness for the Al–0.06Sc–0.02RE alloys compared to Al–0.08Sc.

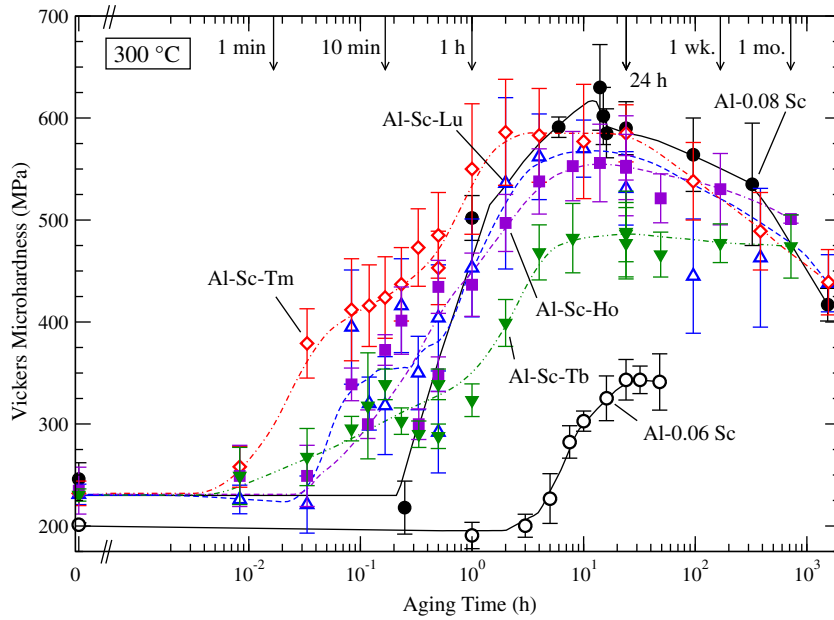


Fig. 1. Vickers microhardness vs. aging time for ternary Al-0.06Sc-0.02RE and binary Al-0.06Sc and Al-0.08Sc (from our prior research [30]) aged at 300 °C. Error bars correspond to 2 SD.

3.3. 3-D LEAP tomographic analyses

3-D LEAP tomographic reconstructed datasets are displayed in Fig. 2a and b for the Al-Sc-Tb and Al-Sc-Tm alloys, for 10 min and 24 h aging conditions, respectively. The higher evaporation field of the trialuminide phase compared to the α -Al matrix results in a local-magnifica-

tion effect, causing a spreading of precipitate atoms in the directions orthogonal to the analysis direction [41–43], which is visible in the reconstructed datasets. Although only Al-Sc-Tb and Al-Sc-Tm are shown, for all four Al-Sc-RE alloys, precipitates rich in Sc and REs are observed in the datasets for 10 min aging, accounting for the initial increase in hardness. After 24 h aging, the precip-

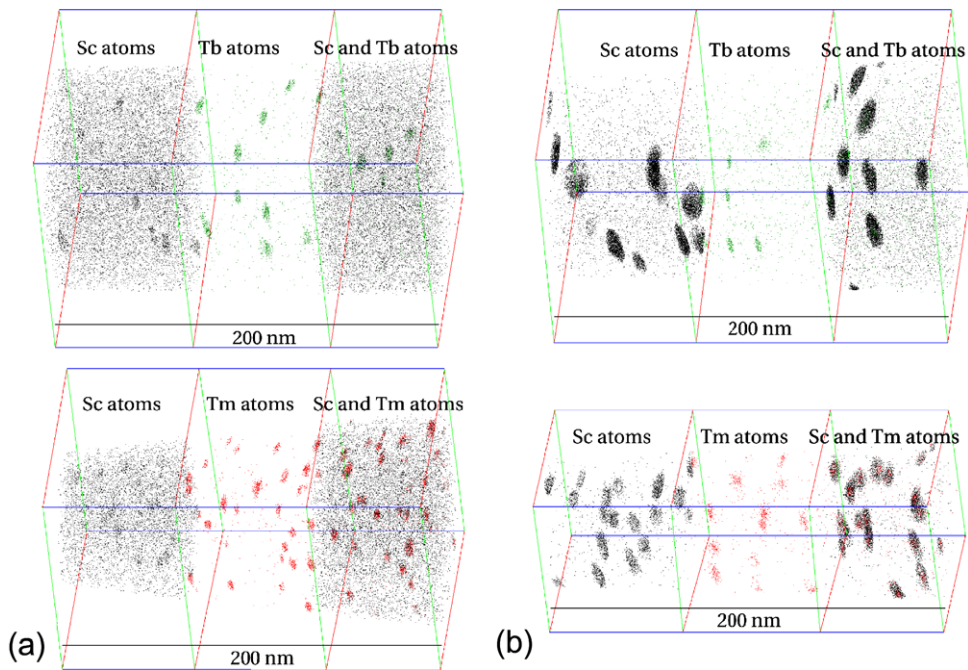


Fig. 2. Three-dimensional LEAP tomographic reconstructions of Al-0.06Sc-0.02Tb and Al-0.06Sc-0.02Tm aged for: (a) 10 min and (b) 24 h at 300 °C. Each reconstruction is divided into three sections, with Sc atoms only displayed in the leftmost section, RE atoms only displayed in the center section, and both Sc and RE atoms displayed in the rightmost section.

itates exhibit a core–shell structure with the REs partitioning strongly to the core, which is surrounded by a Sc-rich shell. Proximity histograms (proxigrams) [44], which give the local concentration as a function of distance from a matrix/precipitate interface averaged over all observed precipitates (between 24 and 86 for these datasets) are shown for precipitates formed after aging for 10 min and 24 h in Fig. 3. They are calculated based on 3 at.% Sc + RE iso-concentration surfaces. Precipitate average compositions are shown as a function of the atomic number of the RE addition (Fig. 4), and are calculated by counting all atoms interior to the matrix–precipitate interface, defined here as the location of the inflection point of the Al concentration curve. Data for Al–0.06Sc–0.02RE, where RE is Gd, Dy, Er or Yb, were generated from experiments performed during a prior investigation [30].

Precipitate statistics were measured from the APT reconstructions (Table 2). The volume fraction, ϕ , of precipitates is calculated from the difference in total and matrix solute concentrations, and assuming that the amount of solute no longer in the α -Al matrix resides in a stoichiometric trialuminide precipitated phase [45]. The lattice parameter of the precipitated phase is approximated by that of Al₃Sc (4.103 Å [39]), and the lattice parameter of the α -Al matrix is approximated by that of pure Al (4.0496 Å [46]). This approach has the advantage of being insensitive to the definition of where the α -Al/precipitate interface is located. The number density of precipitates, N_V , is calculated by counting the number of precipitates included in the analyzed volume (precipitates bisected by boundary of the analysis volume are counted as half of a precipitate), and dividing by the volume of material, which is inferred from the total number of atoms. The average precipitate radius, $\langle R \rangle$, is calculated from the precipitate size distribution (PSD), obtained by applying a modified envelope method to the datasets [47], and approximating the precipitates as spheres. In the determination of $\langle R \rangle$, precipitates bisected by the boundary of the dataset are excluded. Stan-

dard methods for error propagation were employed in calculating the quantities in Table 2 [48].

The PSDs for all alloys, for 10 min and 24 h aging conditions, are shown in Fig. 5, in which the solid vertical bars are the experimental data, and the continuous curves are the Brailsford–Wynblatt (BW) model steady-state PSD [49]. The BW-PSD results from a ϕ -dependent model based on an effective-medium approach in which the net effect of solute adsorption and emission from a randomly distributed array of precipitates is approximated as sources and sinks of solute that are homogeneously distributed throughout the matrix [49,50]. Considering the small number of precipitates measured in some cases, and considering that, at 10 min aging time, ϕ is still evolving (indicating that steady-state coarsening has not yet been achieved), the BW model of precipitate coarsening provides a reasonable prediction of the measured PSDs. Two exceptions are Al–0.06Sc–0.02Ho at 10 min and Al–0.06Sc–0.02Tb at 24 h for which 39 and 24 precipitates were measured, respectively. These datasets have narrower and more sharply peaked PSDs than predicted by the BW coarsening model. In general, agreement between the PSDs measured in the present work and those predicted by the BW model of precipitate coarsening tends to improve with an increasing number of precipitates.

4. Discussion

4.1. Aging microhardness response

An important feature of the age-hardening data (Fig. 1) is the different responses of the ternary Al–0.06Sc–0.02RE alloys compared to the binary Al–0.08Sc alloy at early aging times, <1 h. Scatter in the data at short aging times may be due to local concentration fluctuations of the REs (Table 1), which, although only tens of at. ppm, may constitute a large fraction of the total RE content of these dilute alloys. In all cases, the ternary alloys exhibit

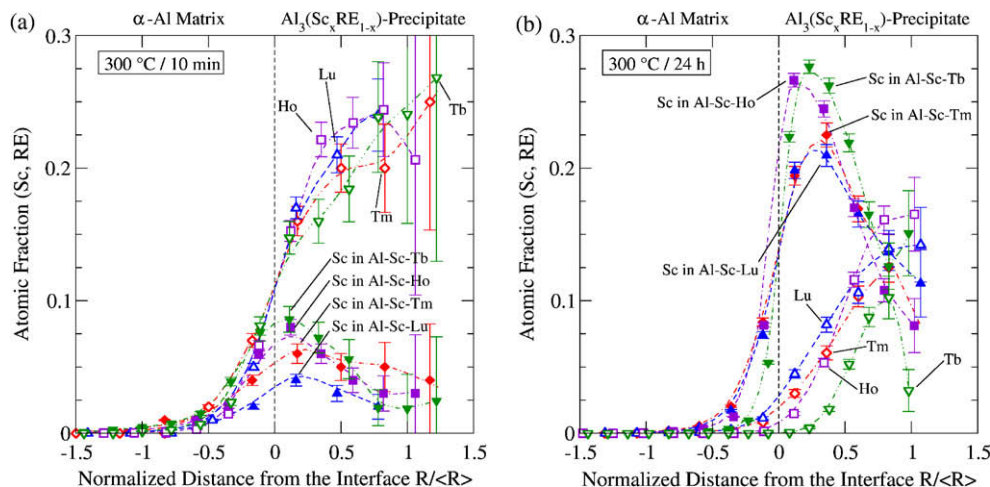


Fig. 3. Proximity histograms of precipitates in Al–0.06Sc–0.02RE aged at 300 °C for: (a) 10 min and (b) 24 h. Error bars correspond to 2 SD.

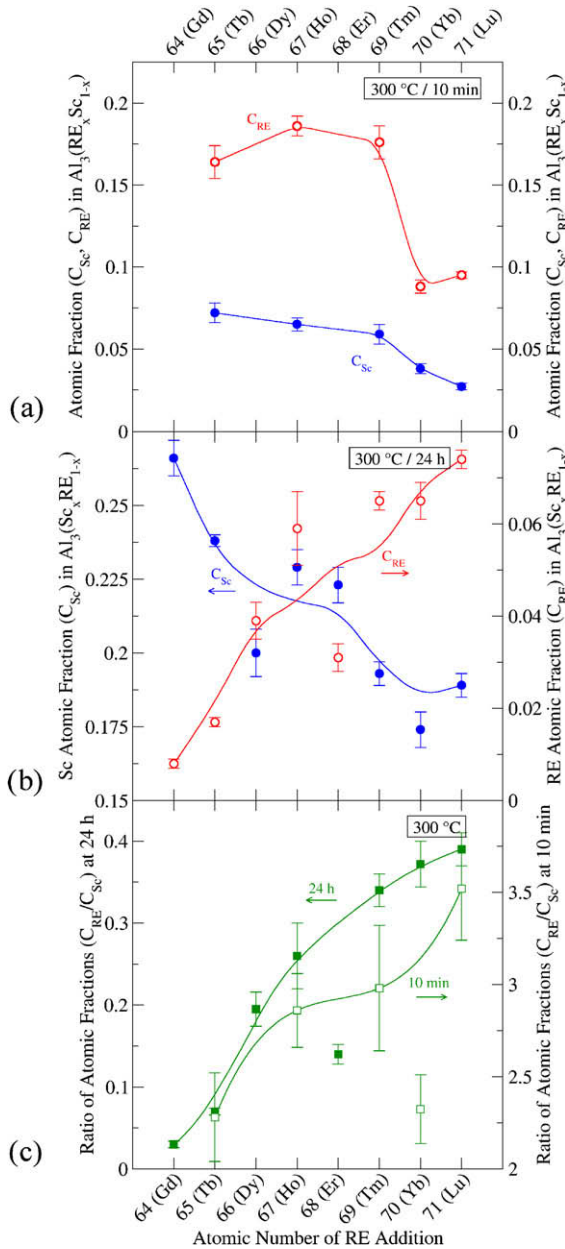


Fig. 4. Solute concentrations (atomic fraction C_{Sc} , C_{RE}) of the $Al_3(Sc_xRE_{1-x})$ precipitates formed in Al-0.06Sc-0.02RE aged at 300 °C for: (a) 10 min and (b) 24 h; and (c) solute concentration ratios (C_{RE}/C_{Sc}) of precipitates formed after aging for 10 min and 24 h. The curves drawn in these plots are intended to be approximate guides for the eye. Precipitate interfaces are defined as the inflection point of the Al concentration curve. Data for Al-0.06Sc-0.02RE (RE = Gd, Dy, Er or Yb) were generated from experiments performed during a prior study [30]. Error bars correspond to 2 SD.

an increase in microhardness much earlier than the binary Al-0.08Sc alloy. In the ternary alloys, the number density of precipitates is $N_V \approx 10^{22} \text{ m}^{-3}$ after only 10 min (Table 2). The proxigrams in Fig. 3 and the precipitate compositions displayed in Fig. 4 indicate that the precipitates formed after 10 min are composed predominantly of $Al_3(RE_{1-x}Sc_x)$, with a minority concentration of Sc. That the precipitates formed after 10 min are RE-rich is also

apparent from Fig. 2. Because the alloys are in either a nucleation or nucleation and growth regime during the initial period of hardening, it is useful to consider the following implications of classical nucleation theory [51,52]:

1. The larger the α -Al/precipitate interfacial free-energy, $\gamma^{\alpha/\beta}$, the longer the incubation time and the smaller the nucleation current (number per unit volume per unit time).
2. The larger the excess chemical free-energy of a supersaturated alloy and the smaller the coherent elastic strain-energy of a precipitate, the shorter the incubation time and therefore the larger the nucleation current.
3. The larger the diffusivity, D , of a solute species, the shorter the incubation time and the larger the nucleation current.

The interfacial free-energy, the excess chemical free-energy for nucleation, and the diffusivities of the RE elements in α -Al are unknown for the ternary alloys studied. In two recent studies, using APT, the coarsening kinetics parameters for dilute binary Al-Yb and Al-Er alloys [31], and a ternary Al-0.06Sc-0.02Er alloy [40] at 300 °C were used to measure $\gamma^{\alpha/\beta}$ and D_{RE} . Data concerning the Al-Yb system are of particular interest because the incubation time of Al-0.06Sc-0.02Yb is very short: a microhardness increase and clustering of Yb atoms are observed in the as-homogenized and quenched state [30,53]. Al-0.06Sc-0.02Er, by contrast, behaves similarly to Al-0.08Sc, with an incubation time of 10–30 min [30]. The α -Al/ Al_3 Yb interfacial free-energy was determined to be $0.6 \pm 0.3 \text{ J m}^{-2}$, that of the α -Al/ Al_3 Er interface to be $0.4 \pm 0.2 \text{ J m}^{-2}$ [31]. For core-shell precipitates in the ternary Al-0.06Sc-0.02Er alloy, where Er partitions to the core and Sc partitions to the shell, the α -Al/ $Al_3(Sc_{1-x}Er_x)$ interfacial free-energy is $0.5 \pm 0.2 \text{ J m}^{-2}$ [40]. These values are larger than the α -Al/ Al_3 Sc interfacial free-energy, calculated to be $0.14\text{--}0.20 \text{ J m}^{-2}$ [54] (with supporting high-resolution electron microscopy observations of Al_3 Sc precipitate faceting [3]), and measured from coarsening and electrical resistivity data to be $0.214\text{--}0.224 \text{ J m}^{-2}$ [55]. Thus, if the incubation time is mainly controlled by the interfacial free-energy, the RE-containing alloys would have longer incubation periods than the binary Al-0.08Sc alloy, which is not observed.

The diffusivities of Yb and Er in α -Al at 300 °C were determined to be $D_{Yb} = 6 \pm 2 \times 10^{-17} \text{ m}^2 \text{ s}^{-1}$, and $D_{Er} = 4 \pm 2 \times 10^{-19} \text{ m}^2 \text{ s}^{-1}$ utilizing APT [31]. These diffusivities are both considerably greater than the diffusivity of Sc in α -Al at 300 °C ($D_{Sc} = 9 \times 10^{-20} \text{ m}^2 \text{ s}^{-1}$ [56]). For a ternary Al-Sc-Er alloy, the diffusivities of Sc and Er at 300 °C are found to be $D_{Sc} = 6 \pm 3 \times 10^{-20} \text{ m}^2 \text{ s}^{-1}$ and $D_{Er} = 9 \pm 6 \times 10^{-22} \text{ m}^2 \text{ s}^{-1}$ [40]. This value of D_{Er} is more than two orders of magnitude smaller than that reported for the binary Al-Er study [31], and is also approximately two orders of magnitude smaller than D_{Sc} . A large difference in the diffusivities of Yb and Sc (three orders of

Table 2

Experimental precipitate statistics, and calculated critical precipitate radii for coherency loss R_c at the α -Al/Al₃(Sc,RE) interface.¹

Alloy	Al-Sc-Tb		Al-Sc-Ho		Al-Sc-Tm		Al-Sc-Lu	
Aging time, t (h)	0.17	24	0.17	24	0.17	24	0.17	24
Number density, N_V (10^{22} m^{-3})	0.8(3)	1.2(5)	1.8(5)	5(1)	7(3)	5(2)	5(2)	7(2)
Volume fraction, ϕ (10^{-3})	0.25(4)	2.25(3)	0.46(4)	2.79(1)	1.2(2)	2.66(9)	1.74(9)	3.41(5)
Average radius, $\langle R \rangle$ (nm)	1.8(6)	3(1)	1.7(7)	2(1)	1.5(5)	2.1(8)	1.6(6)	2.1(9)
Critical radius, R_c (nm) (at 300 °C)	5.4	18.9	5.3	18.9	4.9	18.9	5.5	18.9
R_c (nm) (at 27 °C)	4.5	12.1	4.4	12.1	4.1	12.1	4.5	12.1

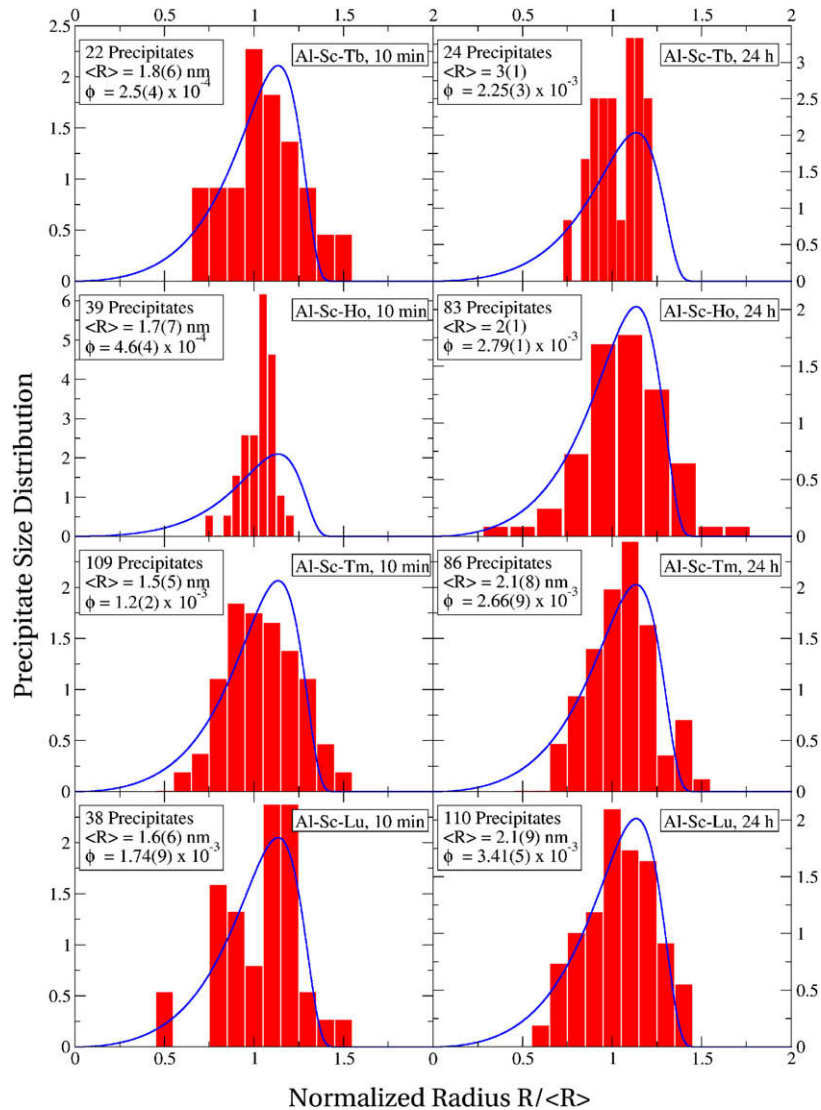
¹ Uncertainty corresponds to 2 SD, and is given in parenthesis after the least significant digits to which it applies.

Fig. 5. Precipitate size distributions (PSDs) for Al-0.06Sc-0.02RE aged at 300 °C for 10 min and 24 h, as represented by solid vertical bars. The Brailsford–Wynblatt model steady-state PSDs are displayed as continuous curves for comparison.

magnitude) is most likely responsible for the short incubation time for the ternary Al-0.06Sc-0.02Yb alloy compared to the binary Al-0.08Sc alloy. By contrast, a difference of one order of magnitude in the diffusivities of Er and Sc does not produce a significant difference in the incubation time for the ternary Al-0.06Sc-0.02Er alloy compared to the Al-0.08Sc alloy [30]. If the total change in free energy associated with nucleation, ($\Delta F_{\text{ch}} + \Delta F_{\text{el}}$), is assumed to

be similar for Al-0.08Sc and Al-0.06Sc-0.02RE, then D_{RE} is the determining factor for the incubation periods of Al-0.06Sc-0.02RE alloys aged at 300 °C. The incubation times and thus the early age-hardening behavior of the present Al-0.06Sc-0.02RE (where RE = Tb, Ho, Tm or Lu) fall between those of Al-0.06Sc-0.02Yb and Al-0.06Sc-0.02Er, suggesting that $D_{\text{Er}} < D_{\text{RE}} < D_{\text{Yb}}$. Ref. [30] indicates that the diffusivity of Yb in α -Al is

anomalously high among the REs explored, based on the shorter incubation time of the Al–0.06Sc–0.02Yb alloy compared to Al–0.08Sc alloy as well as the other Al–0.06Sc–0.02RE alloys studied. The present study demonstrates that a short incubation time for Al–0.06Sc–0.02RE compared to Al–0.08Sc, and therefore a large diffusivity in α -Al relative to that of Sc, is not unique to Yb, but is shared to varying degrees by Tb, Ho, Tm and Lu.

With the exception of Al–Sc–Tm, which achieves its peak microhardness after only ~ 2 h, all the alloys reached their peak microhardness values after ~ 4 – 6 h. The Ho- and Lu-containing alloys exhibit a cross-over point after ~ 1 h: at shorter aging times the aging response of these ternary alloys renders them harder than Al–0.08Sc, while for longer aging times the greater peak strength of Al–0.08Sc is dominant. In the case of Al–Sc–Tm, the cross-over point occurs after ~ 5 h, due to the early increase in microhardness of this alloy, which accelerates the hardening kinetics, effectively shifting the portion of the curve between the initial increase and the peak to earlier times with respect to the Al–0.08Sc. For Al–Sc–Tb, the cross-over point is earlier, as a result of its lower peak microhardness.

4.2. Precipitation strengthening

Because precipitate statistics of the Al–Sc–RE alloys are available at the two aging states for which LEAP tomographic analyses were performed, we can discuss the relationship between microstructure and microhardness increase. It is possible to estimate the precipitate radius at which coherency is lost. Equating the energy of an interfacial dislocation network with the reduction in strain-field energy resulting from a loss of coherency yields the transition radius, R_t [57,58]:

$$R_t = \frac{3\gamma_{dis}(1-\nu)}{2\mu\delta^2(1+\nu)}, \quad (1)$$

where μ and ν are the shear modulus and Poisson ratio of the matrix, respectively, δ is the lattice parameter misfit between the precipitate and matrix, and γ_{dis} is the energy of the interfacial dislocation network per unit area, expressed as:

$$\gamma_{dis} = \frac{\mu b}{2\pi^2} \left\{ 1 + \beta - (1 + \beta^2)^{\frac{1}{2}} - \beta \ln \left[2\beta(1 + \beta^2)^{\frac{1}{2}} - 2\beta^2 \right] \right\} \quad (2)$$

where b is the magnitude of the Burgers vector in the α -Al matrix, and the parameter β is given by $\pi\delta/(1-\nu)$, where δ' is the reduction in lattice parameter misfit due to introducing misfit dislocations [57,58]. This simple calculation is expected to yield a lower bound for R_t , since dislocations need to be nucleated at a coherent interface [59], and this model does not account for this fact. Experimental observations of R_t at elevated temperature (>400 °C) for α -Al/Al₃Sc range from 14 to 25 nm, with 20 nm being typical [3,7,8,55,60–62], and are consistent with the results of this

analysis, which predicts a R_t value of 25 nm at 400 °C. For the 10 min aging time the precipitate lattice parameters for the Al–Sc–RE alloys are chosen assuming they are binary Al₃RE (without Sc) for Tm [63] and Lu [23,26]; for the other two REs the lattice parameters are assumed to have the minimum Sc concentration necessary to stabilize the L1₂ structure, i.e. Al₃(Sc_{0.57}Tb_{0.43}) and Al₃(Ho_{0.72}Sc_{0.28}) [28], and Vegard's law is applied. For an aging time of 24 h, the precipitate shells in contact with the α -Al matrix are nearly pure Al₃Sc and its lattice parameter is used [39]. Increases in temperature and in the α -Al solute concentration both affect the lattice parameter mismatch, and these are accounted for following Ref. [62], with the simplification that the concentrations of Sc and RE in the α -Al matrix, measured by APT, have identical influences on the misfit. Table 2 displays a comparison of the calculated R_t for coherency loss (Eq. (1)) and the experimentally measured precipitate radii. As the experimentally measured precipitate radii are significantly smaller than the calculated transition radii, the precipitates are expected to be coherent with the α -Al matrix. The calculated R_t of the RE-containing precipitates are smaller than those of RE-free precipitates by approximately a factor of 3, owing to the larger lattice parameter misfit when the precipitates contain RE [23,26,28,39,63]. The R_t value is larger at elevated temperatures because of the greater thermal expansion of α -Al as compared to Al₃Sc [64,65].

Since the precipitates are expected to remain coherent, models for ambient-temperature strengthening by coherent precipitates apply. Following Refs. [4,5,19], the strength increment for dislocation–precipitate interactions by order strengthening ($\Delta\sigma_{ord}$), coherency and modulus strengthening ($\Delta\sigma_{coh} + \Delta\sigma_{mod}$), and strengthening by the Orowan bypass mechanism ($\Delta\sigma_{Or}$), and the experimental strength increment, estimated as $\Delta HV/3$ (where ΔHV is the increase in microhardness from the as-quenched state to the aged state), are compared in Table 3 for all four alloys for 10 min and 24 h. For the calculated strength increments, the materials property parameters of the α -Al matrix are approximated by those of pure Al and for the precipitated phases by those of Al₃Sc. For coherency ordering, the lattice parameter mismatch is determined by assuming a stoichiometric trialuminide Al₃(Sc, RE) phase and using the Sc/RE concentration ratio at the precipitate interface, defined as the surface at which the concentration of Al exhibits an inflection point. A linear interpolation is then used between the two closest bounding phase compositions for which lattice parameter data have been reported in Refs. [23,28,63]. In calculating the strength increments, errors were propagated from the precipitate statistics measurements (Table 2).

Strengthening by dislocation shearing of precipitates (order strengthening, $\Delta\sigma_{ord}$) involves the creation of an anti-phase boundary (APB) as well as the approach of a dislocation to the α -Al/precipitate interface through its strain field (coherency and modulus mismatch strengthening, $\Delta\sigma_{coh} + \Delta\sigma_{mod}$). Because these events occur in series,

Table 3
Calculated and experimental strength increments for aged alloys.¹

Alloy	Al–Sc–Tb		Al–Sc–Ho		Al–Sc–Tm		Al–Sc–Lu	
t (h)	0.17	24	0.17	24	0.17	24	0.17	24
$\Delta\sigma_{\text{ord}}$ (MPa)	37(3)	112(1)	50(2)	124(1)	81(6)	121(2)	98(3)	137(1)
$\Delta\sigma_{\text{coh}} + \Delta\sigma_{\text{mod}}$ (MPa)	105(14)	185(20)	130(21)	187(21)	180(25)	191(19)	253(33)	205(20)
$\Delta\sigma_{\text{Or}}$ (MPa)	47(17)	101(45)	67(34)	147(71)	117(52)	147(60)	138(56)	168(68)
$\Delta\text{HV}/3$ (MPa)	36(6)	87(7)	48(9)	107(15)	63(14)	99(14)	30(14)	120(7)

¹ Uncertainty corresponds to 2 SD, and is given in parenthesis after the least significant digits to which it applies.

it is the largest of $\Delta\sigma_{\text{ord}}$ or $\Delta\sigma_{\text{coh}} + \Delta\sigma_{\text{mod}}$ that is applicable for deformation by precipitate shearing. As shearing and bypass of precipitates by dislocations are parallel processes, the process requiring the smaller stress is the operative one. In each case, for both aging conditions, the Orowan bypass mechanism is predicted to be operative, and with the exception of Al–Sc–Lu after 10 min aging, agreement between the models and experiment is reasonable. For the α -Al/ Al_3Sc system, the critical radius value at which the deformation mechanism changes from precipitate shearing to an Orowan bypass mechanism was shown to be 1.5–2.0 nm [4,5]. The experimental values of $\langle R \rangle$ range from 1.5 to 3.3 nm for the alloys in our study. It is therefore not surprising that the experimentally measured strength increments upon aging from the as-quenched state are smaller than the predicted values, as both mechanisms are likely active due to the finite width of the PSDs (Fig. 5), whose standard deviations vary between 0.6 to 1 nm (Table 2). The peak hardness value of Al–Sc–Tb is $\text{HV} = 488 \pm 29$ MPa, which is significantly smaller than the peak microhardness values for Al–Sc–Ho ($\text{HV} = 556 \pm 38$ MPa), Al–Sc–Tm ($\text{HV} = 586 \pm 52$ MPa) and Al–Sc–Lu ($\text{HV} = 570 \pm 28$ MPa) (Fig. 1). This result may be understood in terms of the precipitate statistics. At an aging time of 24 h, the Al–Sc–Tb alloy exhibits a precipitate number density $N_V = 1.2 \pm 0.5 \times 10^{22} \text{ m}^{-3}$ (compared to between $5 \pm 2 \times 10^{22}$ and $7 \pm 2 \times 10^{22} \text{ m}^{-3}$ for the other alloys) and an average precipitate radius $\langle R \rangle = 3 \pm 1$ nm (compared to ~ 2 nm for the other alloys). The smaller N_V value, and hence larger $\langle R \rangle$ value, for Al–Sc–Tb compared to the other alloys results in a smaller stress for dislocations to overcome precipitates by the Orowan bypass mechanism, and therefore a smaller peak microhardness value.

4.3. Precipitate compositions

In Fig. 2, it is clear that after 24 h aging, a core–shell structure has developed, with Tb or Tm partitioning strongly to the precipitate cores, while the surrounding shell is Sc-rich. This is also apparent in the 24 h aging proxigrams (Fig. 3), which exhibit the same behavior for Al–Sc–Ho and Al–Sc–Lu. Comparison of the proxigrams for the 10 min and 24 h aging times reveals a noticeable evolution of the precipitate structures and compositions. After 10 min aging, although the beginning of a core–shell structure is evident with a peak in Sc concentration near the

α -Al/precipitate interface, the precipitates contain predominantly REs. After 24 h aging, however, the precipitates contain more Sc than REs (Fig. 4) and the core–shell structure is well developed. APT experiments at longer aging times are necessary to determine if this effect is kinetic in origin, owing to the early precipitation of RE-rich precipitates and their subsequent engulfment by the slower-diffusing Sc atoms, or if the structure has achieved its thermodynamic equilibrium state, which is unlikely. The lattice parameters of Al_3Tm (4.203 Å [63]) and Al_3Lu (4.191 Å [23]) are both larger than that of Al_3Sc (4.103 Å [39]). Although Tb and Ho do not form stable L_{12} phases with Al unless some Sc is present to stabilize the structure, addition of Tb or Ho to Al_3Sc results in an increased lattice parameter [28]. Consequently, partitioning of RE elements at the precipitate core results in a configuration that minimizes the lattice parameter misfit across the core–shell and shell–matrix interfaces, which reduces the free-energy resulting from lattice strain. Other considerations in the system energetics, such as relative free energies of the α -Al/ Al_3RE , $\text{Al}_3\text{RE}/\text{Al}_3\text{Sc}$ and α -Al/ Al_3Sc heterophase interfaces, and substitutional energies for REs on the Sc sublattice in Al_3Sc , may also play a role in producing the core–shell structure, but are not addressed here, as they require first-principles calculations.

The ratio of solute concentrations in the precipitates, $C_{\text{RE}}/C_{\text{Sc}}$, increases systematically with increasing RE atomic number, from Gd to Lu, for both the RE-rich precipitates at 10 min aging time, and for the Sc-rich precipitates after 24 h aging (Fig. 4c). At an aging time of 24 h, $C_{\text{Er}}/C_{\text{Sc}}$ is smaller than would be anticipated from this trend. Among the late lanthanoids (Er–Lu), which have full solubility in Al_3Sc , Er is unique as Al–0.06Sc–0.02Er does not exhibit a shorter incubation time at 300 °C than Al–0.08Sc. The longer incubation time for Al–0.06Sc–0.02Er may be due to a diffusivity of Er in α -Al that is smaller than, or comparable to, the Sc diffusivity [31,40,56] (and smaller than that of the other late lanthanoids), or to a larger free energy of formation of a nucleus that prolongs the incubation period. In either case, precipitates that form in Al–0.06Sc–0.02Er do not begin as an Er-rich trialuminide which through a Sc addition become subsequently Sc-rich [40], as is the case for the other late lanthanoids. As equilibrium is approached at longer aging times, the slower-diffusing Er atoms migrate to the precipitates, increasing the Er concentration of those precipitates, thereby also increasing $C_{\text{RE}}/C_{\text{Sc}}$ [40]. The overall trend of increasing $C_{\text{RE}}/C_{\text{Sc}}$ is

consistent with the trend of increasing miscibility of the Al_3RE and Al_3Sc phases with increasing RE atomic number [23]. Other factors may be contributing to this effect as well, such as electronic interactions between the RE and Sc in the α -Al matrix, elastic effects arising from the lattice parameter mismatch which varies with atomic number of RE addition [26], or differences in their diffusivities.

5. Conclusions

Four ternary Al–0.08Sc–0.02RE alloys (at.%, RE = Tb, Ho, Tm or Lu) were cast, homogenized at 640 °C, and aged at 300 °C, resulting in nanoscale $\text{Al}_3(\text{Sc}_x\text{RE}_{1-x})$ precipitates responsible for increases in microhardness. The microstructures of the alloys aged for 10 min and 24 h were investigated by 3-D LEAP tomography, yielding the following conclusions:

- The Al–Sc–RE alloys all exhibit a precipitation-hardening response characterized by the four classical stages of incubation, under-aging, peak-aging and over-aging. The peak microhardness values of Al–Sc–Tb and Al–Sc–Ho were lower than the other two ternary alloys and the Al–0.08Sc alloy, due to the smaller volume fraction of the precipitated phase, resulting from the inability to fully solutionize the alloys.
- The incubation period is shorter in the four ternary alloys than in the binary Al–0.08Sc alloy, despite the smaller total solute concentrations in the ternary alloys. Al–Sc–Tm has the shortest incubation period of all investigated alloys (the microhardness increases by 65% after 2 min aging), and displays evidence, together with the other three binary alloys, of a bimodal microhardness increase, as was observed earlier for Al–Sc–Yb [30]. By analogy to this system, it is likely that the REs in this study have larger diffusivities in α -Al at 300 °C than does Sc.
- Trialuminide $\text{Al}_3(\text{RE}_{1-x}\text{Sc}_x)$ precipitates, which form at 10 min aging time and are responsible for the first hardness peak, contain a larger RE concentration than Sc. At 24 h aging time (near the second microhardness peak), the $\text{Al}_3(\text{Sc}_{1-x}\text{RE}_x)$ precipitates have grown, they contain a larger Sc concentration than RE, and they have a core–shell structure with the REs partitioning strongly at the cores of the precipitates.
- Through at least 24 h aging time, the precipitates are expected to remain coherent with the α -Al matrix. Simple strengthening models predict that dislocations bypass the precipitates by the Orowan strengthening mechanism at both the 10 min and 24 h aging times, and exhibit reasonable agreement with experimentally measured microhardness values.

Acknowledgments

This research is supported by the US Department of Energy, Office of Basic Energy Sciences, through Grant DE-FG02-98ER45721. The LEAP tomograph was purchased

with funding from the NSF-MRI (Grant DMR-0420532) and ONR-DURIP (Grant N00014-0400798) programs. Research Assistant Professor D. Isheim is thanked for managing NUCAPT. Drs. R.A. Karnesky and M.E. van Dalen are thanked for helpful discussions and access to unpublished data.

Appendix A. Laser energy selection

Accurate and quantitative compositional analyses performed employing APT with electrical pulsing depends on the experimental conditions, including crystallographic orientation [66,67], evaporation rate [68], specimen temperature and pulse fraction [69]. After careful studies of these experimental variables, which are specific to the system being studied, it is possible to perform reliable quantitative APT analyses [70,71]. Although pulsed-voltage APT is a technique that continues to be used, pulsed laser atom-probe (PLAP) tomography offers a number of distinct advantages, including allowing APT analysis of materials with poor electrical conductivities [36,72–74], and a high mass resolving power ($m/\Delta m$) if care is taken to select optimal laser pulse parameters [75,76]. Also, whereas pulsed-voltage APT results in the specimen being subjected to a cyclical stress state, PLAP tomography is conducted at a steady-state voltage resulting in a static stress state, which extends the life of a specimen, thereby increasing the size of the data sets.

Because the laser pulse energy can have a significant effect on the quality of the data collected, including the accuracy of the measured composition [77], it is critical to select the optimal laser pulse energy. To determine an appropriate laser pulse energy, a specimen was prepared from Al–0.06Sc–0.02Lu in the homogenized and quenched condition, which is assumed to be representative of the dilute alloys studied. The conditions of field evaporation are identical to those described in Section 2 ($T = 30$ K, pulse repetition rate = 500 kHz), except that the laser energy was varied from 0.5 to 5 nJ pulse^{−1}, to assess its effect on the measured composition. The evaporation rate was maintained at 3%, and the steady-state voltage was 4.0–4.4 kV (PLAP) and 5.0–5.2 kV (voltage pulsing). The same micro-tip was used for all measurements, which consisted of datasets of 5×10^6 ions each. The PLAP datasets were collected in order of increasing laser energy. The data set at zero laser energy corresponds to voltage pulsing at a pulse fraction of 15%; this was the last dataset collected, directly following the 5 nJ pulse^{−1} data set.

The measured alloy composition as a function of laser energy is presented in Fig. A1. The error bars correspond to 2 SD. The concentrations of Sc and Lu measured by PLAP are constant in the range of 0.5–5 nJ pulse^{−1}. The concentration of Sc is approximately constant at 622 ± 24 to 646 ± 24 at. ppm, and the concentration of Lu varies from 173 ± 14 to 210 ± 16 at. ppm. The measured Sc concentration using voltage pulsing is 617 ± 24 at. ppm and that of Lu is 168 ± 14 at. ppm; both values

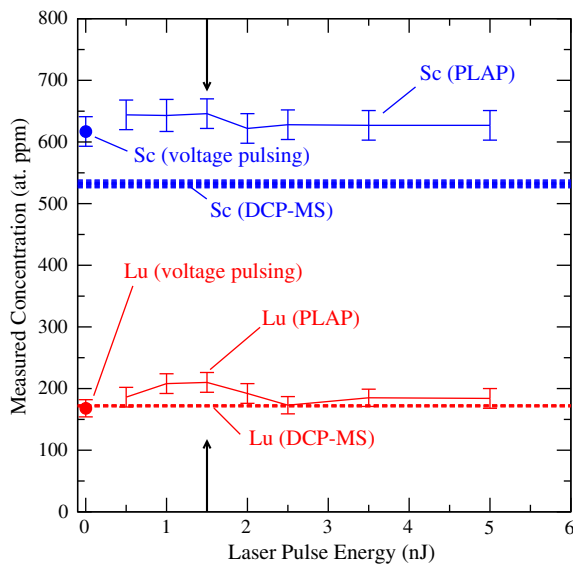


Fig. A1. Measured composition of Al-0.06Sc-0.02Lu as a function of laser energy per pulse. The analysis temperature was 30 ± 2 K. The data at 0 nJ correspond to a dataset collected using voltage pulsing, at a pulse fraction of 15%. Dashed lines indicate the results of bulk chemical analysis by DCPMS. The thicknesses of the dashed lines correspond to the measured DCPMS compositions ± 2 SD. Black arrows mark the laser energy used in the present work: $1.5 \text{ nJ pulse}^{-1}$.

are within the corresponding concentrations measured by PLAP to within 2 SD. No systematic or significant variation in concentration with laser energy occurs between 0.5 and 5 nJ pulse^{-1} . The bulk concentrations of Sc and Lu, as determined using DCPMS (Table 1, Section 3.1) are displayed in Fig. A1, as dashed lines, the thicknesses of which correspond to ± 2 SD in the measurements. The Sc concentration as determined by DCPMS is smaller than the Sc concentration as determined by PLAP or voltage-pulsed APT, but this is not true of the Lu concentration, which is nearly identical for all methods. The smaller Sc concentration, when measured by DCPMS, is expected to be a result of the larger sampling volume with this technique compared to APT or PLAP: DCPMS is insensitive to composition fluctuations at the nanometer scale, while these fluctuations are measurable by APT/PLAP. The laser energy used for all results presented in the main text is $1.5 \text{ nJ pulse}^{-1}$; this yields accurate and quantitative compositional results.

References

- [1] Røyset J, Ryum N. *Int Mater Rev* 2005;50:19.
- [2] Toropova LS, Eskin DG, Kharakterova ML, Dobatkina TV. *Advanced aluminum alloys containing scandium: structure and properties*. London: Gordon & Breach; 1998.
- [3] Marquis EA, Seidman DN. *Acta Mater* 2001;49:1909.
- [4] Seidman DN, Marquis EA, Dunand DC. *Acta Mater* 2002;50:4021.
- [5] Marquis EA, Seidman DN, Dunand DC. *Acta Mater* 2003;51:285.
- [6] Hyland Jr RW. *Metall Mater Trans A* 1992;23:1947.
- [7] Drits MY, Ber LB, Bykov YG, Toropova LS, Anastas'eva GK. *Phys Met Metallogr* 1984;57:118.

- [8] Iwamura S, Miura Y. *Acta Mater* 2004;52:591.
- [9] Fuller CB, Seidman DN, Dunand DC. *Scripta Mater* 1999;40:691.
- [10] Blake N, Hopkins MA. *J Mater Sci* 1985;20:2861.
- [11] Novotny GM, Ardell AJ. *Mater Sci Eng A* 2001;318:144.
- [12] Clouet E, Barbu A, La L, Martin G. *Acta Mater* 2005;53:2313.
- [13] Røyset J, Ryum N. *Mater Sci Eng A* 2005;396:409.
- [14] Marquis EA, Seidman DN, Dunand DC. *Acta Mater* 2003;51:4751.
- [15] Marquis EA, Seidman DN, Dunand DC. *Microstructural, and creep properties of an Al-2Mg-0.2Sc (wt.%) alloy*. In: Zin J, Beaudoin A, Bieler TA, Radhakrishnan B, editors. *Hot deformation of aluminum alloys III*. Warrendale, PA: TMS; 2003. p. 177.
- [16] Marquis EA, Seidman DN, Asta M, Woodward C, Ozolins V. *Phys Rev Lett* 2003;91:036101:1.
- [17] Marquis EA, Seidman DN. *Surf Interface Anal* 2004;36:559.
- [18] Marquis EA, Seidman DN, Asta M, Woodward C. *Acta Mater* 2006;54:119.
- [19] Fuller CB, Seidman DN, Dunand DC. *Acta Mater* 2003;51:4803.
- [20] van Dalen ME, Dunand DC, Seidman DN. *Acta Mater* 2005;53:4225.
- [21] Fuller CB, Murray JL, Seidman DN. *Acta Mater* 2005;53:5401.
- [22] Fuller CB, Seidman DN. *Acta Mater* 2005;53:5415.
- [23] Harada Y, Dunand DC. *Mater Sci Forum* 2007;539–543:1565.
- [24] Sawtell RR, Morris J. *Dispersion strengthened aluminum alloys*. Warrendale: TMS; 1988. p. 409.
- [25] Sawtell RR. *Exploratory alloy development in the system Al-Sc-X*. Ph.D. Thesis, University of California, Berkeley; 1988.
- [26] Harada Y, Dunand DC. *Intermetallics* 2009;17:17.
- [27] Knipling KE, Dunand DC, Seidman DN. *Z Metallkd* 2006;97:246.
- [28] Zalutskaya OI, Ryabov VR, Zalutsky II. *Dopovidi Akademii Nauk Ukrainkoi RSR Seriya A-Fiziko-Matematichni Ta Technichni Nauki* 1969:255.
- [29] Zalutskaya OI, Kotsevov VG, Karamyshev NI, Ryabov VR, Zalutsky II. *Dopovidi Akademii Nauk Ukrainkoi RSR Seriya A-Fiziko-Matematichni Ta Technichni Nauki* 1970:751.
- [30] Karnesky RA, van Dalen ME, Dunand DC, Seidman DN. *Scripta Mater* 2006.
- [31] van Dalen ME, Karnesky RA, Cabotaje JR, Dunand DC, Seidman DN. *Acta Mater* 2009;57:4081.
- [32] Naumov A. *Russ J Non-ferrous Met* 2008;49:14.
- [33] Seidman DN. *Annu Rev Mater Res* 2007;37:127.
- [34] Seidman DN. *Rev Sci Instrum* 2007;78:030901:1.
- [35] Kelly TF, Miller MK. *Rev Sci Instrum* 2007;78:031101:1.
- [36] Tsong TT. *Surf Sci* 1978;70:211.
- [37] Wada M. *Surf Sci* 1984;145.
- [38] Danoix F, Grancher G, Bostel A, Blavette D. *Ultramicroscopy* 2007;107:739.
- [39] Murray JL. *J Phase Equilib* 1998;19:380.
- [40] Karnesky RA, Dunand DC, Seidman DN. *Acta Mater* 2009;57:4022.
- [41] Miller MK, Hetherington MG. *Surf Sci* 1991;246:442.
- [42] Vurpillot F, Bostel A, Blavette D. *Appl Phys Lett* 2000;76:3127.
- [43] Marquis EA, Vurpillot F. *Microsc Microanal* 2008;14:561.
- [44] Hellman OC, Vandenbroucke JA, Rusing J, Isheim D, Seidman DN. *Microsc Microanal* 2000;6:437.
- [45] van Dalen ME, Seidman DN, Dunand DC. *Acta Mater* 2008;56:4369.
- [46] Pearson WB. *A handbook of lattice spacings and structures of metals and alloys*. London: Pergamon Press; 1967.
- [47] Miller MK, Kenik EA. *Microsc Microanal* 2004;10:336.
- [48] Bevington PR, Robinson DK. *Data reduction and error analysis for the physical sciences*. New York: McGraw-Hill; 2002.
- [49] Brailsford AD, Wynblatt P. *Acta Metall* 1979;27:489.
- [50] Ratke L, Voorhees PW. *Growth and coarsening: Ostwald ripening in material processing*. Berlin: Springer Verlag; 2002.
- [51] Wagner R, Kampmann R, Voorhees PW. *Homogeneous second-phase precipitation*. In: Kostorz G, editor. *Phase transformations in materials*, vol. 5. New York: Wiley; 2001. p. 309.
- [52] Martin G. *Solid state phase transformation in metals and alloys*. Orsay: Les Editions de Physique; 1978.

- [53] van Dalen ME. Microstructure and creep properties of Al–Sc alloys micro-alloyed with Lanthanides (Yb or Gd) and transition metals (Ti or Zr). Ph.D. Thesis, Northwestern University; 2007.
- [54] Asta M, Ozolins V, Woodward C. *JOM* 2001;53:16.
- [55] Watanabe C, Kondo T, Monzen R. *Metall Mater Trans A* 2004;35:3003.
- [56] Fujikawa S-I. *Diffusion in materials: Dimat-96*, vols. 143–147. Zurich: Trans Tech; 1997. p. 115.
- [57] Jesser W. *Philos Mag* 1969;19:993.
- [58] Shiflet G. *Mater Sci Eng* 1986;81:61.
- [59] Isheim D, Seidman DN. *Metall Mater Trans A* 2002;33:2317.
- [60] Riddle YW, Sanders Jr TH. *Mater Sci Forum* 2000;331–337:939.
- [61] Jones MJ, Humphreys FJ. *Acta Mater* 2003;51.
- [62] Røyset J, Ryum N. *Scripta Mater* 2005;52:1275.
- [63] Cannon JF, Hall HT. *J Less Common Met* 1975;40:313.
- [64] Touloukian Y, Kirby R, Taylor R, Desai P, editors. *Thermal expansion: metallic elements and alloys*. New York: Plenum; 1975.
- [65] Harada Y, Dunand DC. *Scripta Mater* 2003;48:219.
- [66] Yamamoto M, Seidman DN. *Surf Sci* 1983;129:281.
- [67] Macrander AT, Yamamoto M, Seidman DN, Brenner SS. *Rev Sci Instrum* 1983;54:1077.
- [68] Wagner A, Seidman DN. *J Phys* 1986;47:415.
- [69] Herschitz R, Seidman DN. *Surf Sci* 1983;130:63.
- [70] Jang H, Chan DK, Seidman DN, Merkle KL. *Scripta Metall Mater* 1993;29:69.
- [71] Jang H, Shashkov DA, Chan DK, Seidman DN. *Scripta Metall Mater* 1994;30:663.
- [72] Kelly TF, Larson DJ, Thompson K, Alvis RL, Bunton JH, Olson JD, et al. *Annu Rev Mater Res* 2007;37:681.
- [73] Kellogg GL, Tsong TT. *J Appl Phys* 1980;51:1184.
- [74] Kellogg GL. *J Phys E* 1987;20.
- [75] Bunton JH, Olson JD, Lenz DR, Kelly TF. *Microsc Microanal* 2007;13:418.
- [76] Cerezo A, Clifton PH, Gomberg A, Smith GDW. *Ultramicroscopy* 2007;107:720.
- [77] Zhou Y, Booth-Morrison C, Seidman DN. *Microsc Microanal* 2008;14:571.